



Article

Iron and Carbon Isotope Constraints on the Formation Pathway of Iron-Rich Carbonates within the Dagushan Iron Formation, North China Craton

Xiaoxue Tong ^{1,2,3}, Kaarel Mänd ^{4,5} , Yuhao Li ⁴, Lianchang Zhang ^{1,2,3}, Zidong Peng ^{1,2,3}, Qiang Wu ⁶, Pengbo Li ⁶, Mingguo Zhai ^{1,2,3}, Leslie J. Robbins ⁷ , Changle Wang ^{1,2,3,*} and Kurt O. Konhauser ⁴

- ¹ Key Laboratory of Mineral Resources, Institute of Geology and Geophysics, Chinese Academy of Sciences, Beijing 100029, China; xiaoxuetong1993@mail.iggcas.ac.cn (X.T.); lc Zhang@mail.iggcas.ac.cn (L.Z.); pengzidong2007@126.com (Z.P.); mgzhai@mail.iggcas.ac.cn (M.Z.)
- ² Innovation Academy for Earth Science, Chinese Academy of Sciences, Beijing 100029, China
- ³ University of Chinese Academy of Sciences, Beijing 100049, China
- ⁴ Department of Earth and Atmospheric Sciences, University of Alberta, Edmonton, AB T6G 2E3, Canada; kaarel.mand@ualberta.ca (K.M.); yuhao3@ualberta.ca (Y.L.); kurtk@ualberta.ca (K.O.K.)
- ⁵ Department of Geology, University of Tartu, 50114 Tartu, Estonia
- ⁶ Liaoning Metallurgical Geological Exploration Research Institute Company, Anshan 114000, China; 13998068791@163.com (Q.W.); lipengbodeyouxiang@126.com (P.L.)
- ⁷ Department of Geology, University of Regina, Regina, SK S4S 0A2, Canada; Leslie.Robbins@uregina.ca
- * Correspondence: wangcl@mail.iggcas.ac.cn



Citation: Tong, X.; Mänd, K.; Li, Y.; Zhang, L.; Peng, Z.; Wu, Q.; Li, P.; Zhai, M.; Robbins, L.J.; Wang, C.; et al. Iron and Carbon Isotope Constraints on the Formation Pathway of Iron-Rich Carbonates within the Dagushan Iron Formation, North China Craton. *Minerals* **2021**, *11*, 94. <https://doi.org/10.3390/min11010094>

Received: 28 December 2020

Accepted: 15 January 2021

Published: 19 January 2021

Publisher's Note: MDPI stays neutral with regard to jurisdictional claims in published maps and institutional affiliations.



Copyright: © 2021 by the authors. Licensee MDPI, Basel, Switzerland. This article is an open access article distributed under the terms and conditions of the Creative Commons Attribution (CC BY) license (<https://creativecommons.org/licenses/by/4.0/>).

Abstract: Banded iron formations (BIFs) are enigmatic chemical sedimentary rocks that chronicle the geochemical and microbial cycling of iron and carbon in the Precambrian. However, the formation pathways of Fe carbonate, namely siderite, remain disputed. Here, we provide photomicrographs, Fe, C and O isotope of siderite, and organic C isotope of the whole rock from the ~2.52 Ga Dagushan BIF in the Anshan area, China, to discuss the origin of siderite. There are small magnetite grains that occur as inclusions within siderite, suggesting a diagenetic origin of the siderite. Moreover, the siderites have a wide range of iron isotope compositions ($\delta^{56}\text{Fe}_{\text{Sd}}$) from -0.180‰ to $+0.463\text{‰}$, and a relatively negative C isotope composition ($\delta^{13}\text{C}_{\text{Sd}} = -6.20\text{‰}$ to -1.57‰). These results are compatible with the reduction of an Fe(III)-oxyhydroxide precursor to dissolved Fe(II) through microbial dissimilatory iron reduction (DIR) during early diagenesis. Partial reduction of the precursor and possible mixing with seawater Fe(II) could explain the presence of siderite with negative $\delta^{56}\text{Fe}$, while sustained reaction of residual Fe(III)-oxyhydroxide could have produced siderite with positive $\delta^{56}\text{Fe}$ values. Bicarbonate derived from both DIR and seawater may have provided a C source for siderite formation. Our results suggest that microbial respiration played an important role in the formation of siderite in the late Archean Dagushan BIF.

Keywords: banded iron formation; siderite; dissimilatory iron reduction (DIR); iron isotopes; carbon isotopes; North China Craton

1. Introduction

Banded iron formations (BIFs) are chemical sedimentary rocks composed of iron-rich (total iron >15 wt.%) and silica-rich bands [1–3] that were commonly precipitated during the Archean and Paleoproterozoic. BIFs reflect not only the massive extent of iron (Fe) cycling and deposition during the Precambrian, but they also record critical information about ancient seawater geochemistry and the different (bio)chemical pathways through which the atmosphere–biosphere–hydrosphere systems have been linked throughout Earth's history [4–7]. Four mineralogical end-member facies of BIF have been described based on the characteristic Fe-bearing mineral assemblages, including (i) oxides (hematite, magnetite), (ii) carbonates (siderite, ankerite), (iii) silicates (e.g., greenalite, cummingtonite,

grunerite), and (iv) sulfides (pyrite). Sulfide facies is not generally used to study sedimentary environments, as it is composed mainly of pyritic carbonaceous shale or slate and does not represent a chemical precipitate [2,3,8]. The abundance and distribution of these facies have been used to infer environmental conditions during deposition and subsequent sedimentary–diagenetic–metamorphic evolutionary processes [1–3,8].

Amongst these four facies, the carbonate facies provide the most valuable insights on the origin and coupled cycling of Fe and carbon (C) in BIFs [9]. Siderite is the major Fe-rich component in the carbonate facies of BIFs and its formation requires anoxic, ferruginous conditions, high alkalinity, and low sulfate concentrations [10–12]. Despite significant scientific interest and research, there is still no consensus on the origin of siderite, and two main formation pathways are proposed [13–19]. First, in Archean oceans where Fe(II) and HCO_3^- concentrations would have been high and the prevailing redox conditions were reducing [20–23], the direct precipitation of siderite from seawater may have been feasible [13,22,24,25]; however, Jiang and Tosca [26] have suggested that seawater siderite precipitation may have been kinetically unfavorable. Seawater-like carbon isotopes ($\delta^{13}\text{C} \sim 0\text{‰}$) of siderite in some BIFs have been taken as evidence to support this direct precipitation pathway [25,27]. Second, microbial dissimilatory iron reduction (DIR) during early diagenesis has been shown to be a viable formation pathway for siderite formation based primarily on the relatively negative $\delta^{13}\text{C}$ and highly variable $\delta^{56}\text{Fe}$ values of many siderites, as well as experimental simulations [16,28–33]. In particular, siderites in the ~2.5 Ga Brockman Iron Formation in Hamersley, Australia [30] and in the BIFs of the ~3.8 Ga Isua Supracrustal Belt, Greenland [31] are proposed to have been precipitated through DIR. Moreover, siderites have also been suggested to form through the ageing and transformation of green rust [34] and through the reaction of Fe(III) minerals and organic carbon (C_{org}) at elevated burial temperatures and pressures (e.g., $\geq 170\text{ °C}$ and $\geq 1.2\text{ kbar}$) [17,19,35].

Interestingly, siderites are generally more common in Superior-type than Algoma-type BIFs, which may reflect the commonly lower metamorphic grade in Superior-type BIFs. An exception to this is the Dagushan BIF (~2.53–2.51 Ga) in the Anshan area, North China Craton (NCC), where siderites are widely distributed. The Dagushan BIF is the first Algoma-type BIF to be reported that has retained a series of relatively integrated depositional facies, including carbonate, oxide, and silicate facies [36]. The relatively mild metamorphic grade (greenschist- to lower amphibolite-facies) compared to typical Archean rocks (typically amphibolite-facies) also makes the Dagushan BIF a good target for examining the sources of C and Fe and the mechanisms that transformed them to siderite. Here, we report an integrated petrographic and C and Fe isotopic study on the siderites of the Dagushan BIF in order to constrain the formation pathway. We compare our results to other siderite-forming pathways proposed for different geological periods in order to provide new constraints on C and Fe cycling through time.

2. Geological Setting

The Dagushan BIF is situated in the Anshan area of the Eastern Block of the NCC (Figure 1). The Anshan Group (~2.56–2.53 Ga) can be divided into two distinct units; the (1) Anshan and (2) Benxi units (Figure 1b) [37–43]. The Anshan unit has an upper greenschist- to lower amphibolite-facies metamorphic grade, and is dominated by ~2530 Ma BIFs (e.g., the Dagushan, Dong’anshan, and Qidashan BIFs), siliciclastic meta-sedimentary rocks, and minor metavolcanic rocks [44]. These meta-sedimentary rocks are composed of chlorite-quartz schist, biotite gneiss, mica-quartz schist, and phyllite [43,44]. By contrast, the Benxi unit is of a relatively higher metamorphic grade (amphibolite-facies), and mostly consists of ca. 2563 to 2530 Ma BIFs (e.g., Gongchangling, Beitai, Waitoushan, and Nanfen BIFs), as well as basic to felsic volcanic rocks with lesser volcanoclastic and siliciclastic sedimentary rocks [42,44].

Located in the Anshan unit, the Dagushan BIF is an Algoma-type BIF that was deposited in a back-arc basin [43,44]. Age constraints on the Dagushan BIF are provided by

weighted mean U-Pb ages from the youngest group of detrital zircons from the intercalated meta-greywacke, coupled with the maximum metamorphic age of ~ 2.51 Ga in the Anshan-Benxi area. It is suggested that the Dagushan BIF was deposited between 2.53 and 2.51 Ga [43], in accordance with the ages of other BIFs in the Anshan unit [42,45].

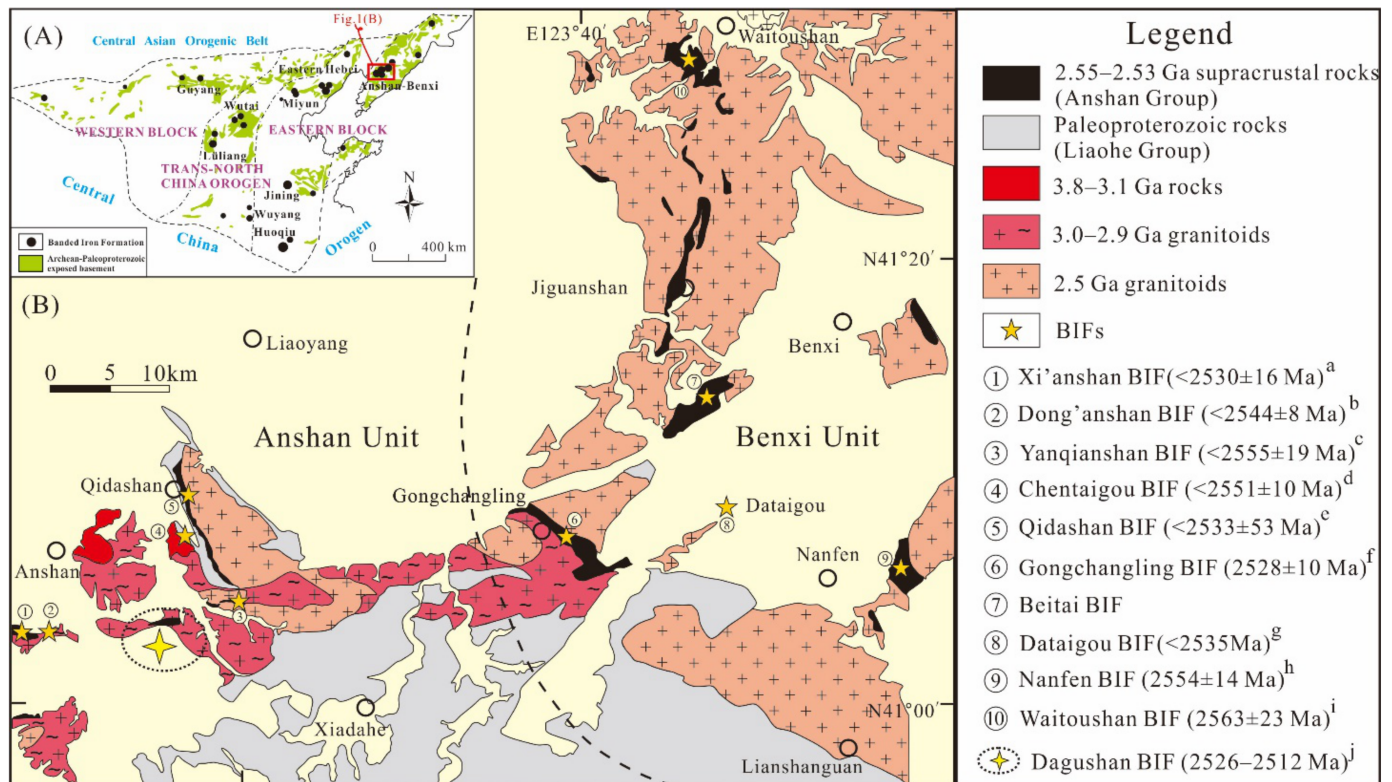


Figure 1. (A) Subdivisions of the North China Craton (NCC) showing the location of the Anshan-Benxi area and distribution of major Banded Iron Formations (BIFs) (modified from [46,47]); (B) geological sketch map of the Anshan-Benxi area indicating the study area (modified from [40]). Numbers show previous U-Pb zircon ages of supracrustal rocks associated with the BIFs. Age data sources: a—[45]; b—[48]; c—[49]; d—[39]; e—[42]; f—[38]; g—[50]; h—[41]; i—[51]; j—[43].

Three distinctive sedimentary facies are recognized in the Dagushan BIF: (1) an oxide facies, mainly composed of magnetite; (2) a silicate facies, composed of cummingtonite, stilpnomelane, and chlorite (silicate $> 20\%$); (3) a carbonate facies, with siderite as the dominant Fe-bearing phase. As the major constituent ($\sim 50\%$ vol.%) of the Dagushan BIF, the silicate facies BIF is distributed mainly in the south of the formation (Figure 2), and the oxide-facies BIF occurs primarily in the middle of the formation, making up to ca. 30 vol.% of the total BIF. The carbonate facies accounts for the remaining 20 vol.% of the Dagushan BIF and is spread predominantly over the northern region.

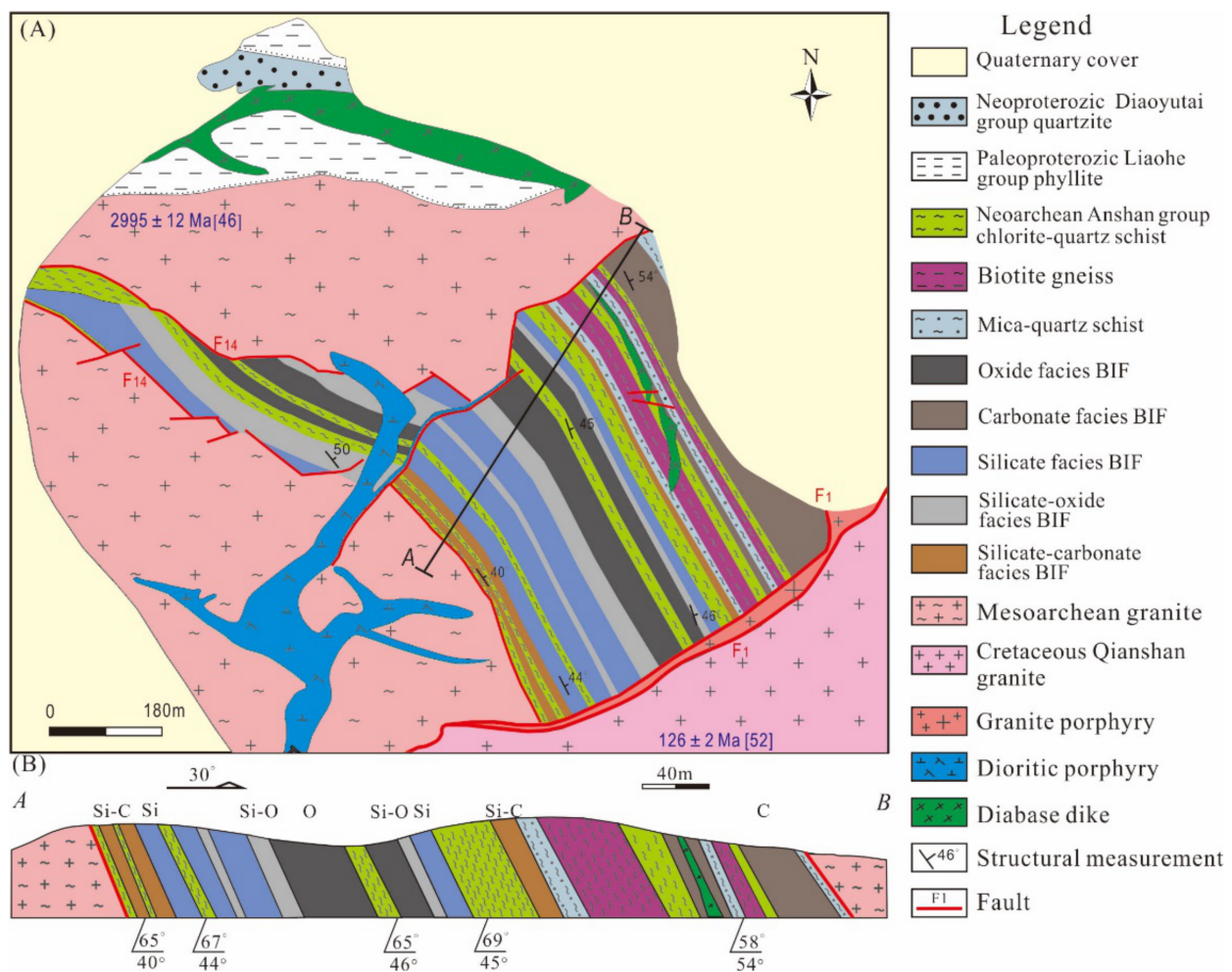


Figure 2. (A) Geological map of the Dagushan iron deposit (modified after [36]) including the main three depositional facies: O—oxide; Si—silicate; C—carbonate. (B) A cross-section of the Dagushan deposit, indicating the general stratigraphy of the Dagushan BIF and associated rocks. Transitional facies exist between the principal ones due to gradual facies transitions: silicate-oxide facies (Si-O) and silicate-carbonate facies (Si-C). For the purposes of this study, Si-O facies is merged into the silicate facies and Si-C into the carbonate facies.

The Dagushan BIF is associated with well-bedded chlorite-quartz schist, biotite gneiss, and minor mica-quartz schist (Figure 2) [43]. The beds strike north-west and dip 40–70° to north-east, and some of these supracrustal rocks are cross-cut by quartz and calcite veins that indicate later-stage hydrothermal alteration. Igneous rocks extend widely in the study area, consisting predominantly of Mesoarchean granite, Cretaceous granite, granite porphyry, diorite porphyrite, and diabase dikes (Figure 3a). The ~3.0 Ga Mesoarchean granite (Donganshan granite, [51]), is on the footwall of the Neoproterozoic supracrustal rocks (Figures 2 and 3b). All field observations indicate a fault contact between it and the BIF. The Cretaceous granite (Qianshan granite, [52]), as well as granite porphyry, shows evident unconformable contact relationships with the Dagushan supracrustal rocks.

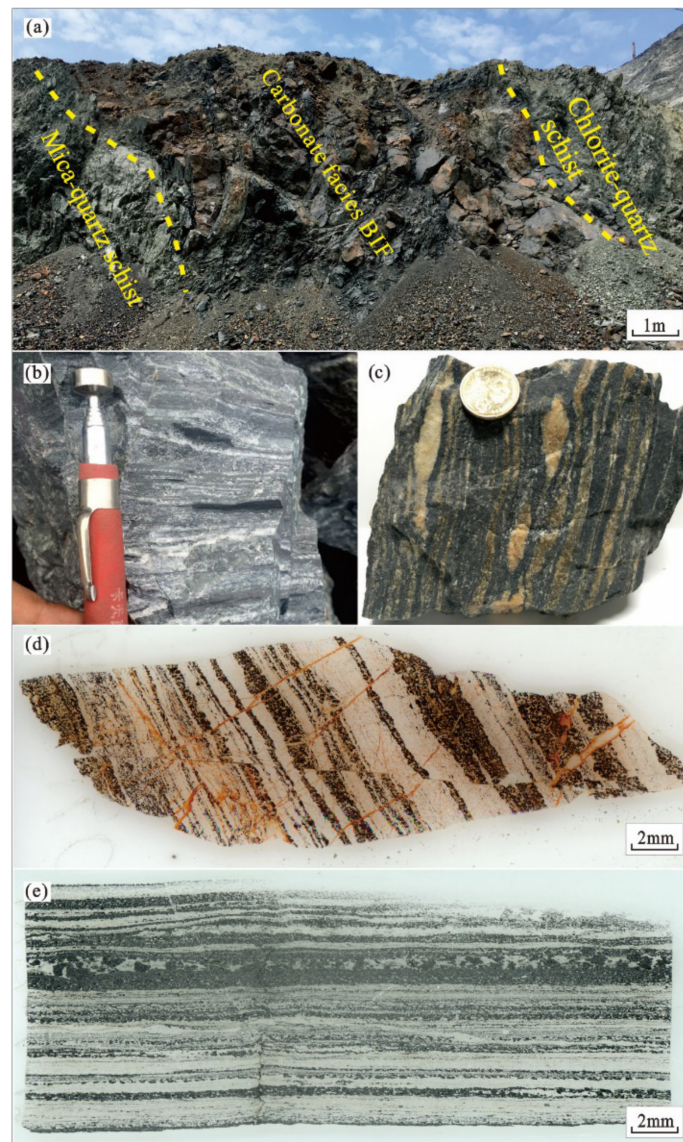


Figure 3. (a) Field relationships of carbonate facies BIF and its associated rocks in the Dagushan iron deposit. Yellow dashed lines represent lithologic boundaries. (b) Fresh hand specimen of carbonate facies BIF with black and buff-white micro bands. (c) Weathered hand specimen of carbonate facies BIF, showing rotational porphyroclasts with right shearing characteristics. (d) Iron- and carbonate-rich bands with brown to yellow fractures. (e) Alternating buff-white and black microbands with gradational contacts, comprising siderite, quartz, and magnetite in varying proportions.

3. Analytical Methods

Samples were obtained from open pit outcrops in the northern part of the Dagushan iron mine (41°03'10" N, 123°03'27" E). Detailed petrographic examinations using transmitted and reflected light were carried out to determine the mineralogy and paragenetic history of all BIF samples. Scanning electron microscopy equipped with energy dispersive spectrometry (SEM-EDS) was used to examine small-scale relationships between textures and measure elemental abundances at the Institute of Geology and Geophysics, Chinese Academy of Sciences in Beijing (IGGCAS). Major element compositions of siderite were determined by wavelength dispersive spectrometry using a JEOL JXA8100 electron probe microanalyzer (EPMA) at the IGGCAS, Beijing. The analyses were carried out at an accelerating voltage of 15 kV and a beam spot diameter of 5 μm with a 20 nA beam current and a 10–30 s counting time on peak. The analytical precision for most elements is estimated to be better than 1.5%.

Ten representative carbonate facies samples were chipped with a hammer to remove weathered surfaces and cleaned with ultrapure water (1.82 MΩ cm). Pure siderite mineral separates were obtained using standard density and magnetic techniques, and then powdered to ~200 μm fineness in an agate mill in order to avoid any metal contact before further geochemical analysis. The agate mill was cleaned with deionized water and alcohol between each sample.

Iron isotope analyses for siderite were conducted at the Laboratory of Isotope Geology, Institute of Geology, Chinese Academy of Geological Sciences. A detailed description of the sample dissolution, chemical separation, and Fe isotope analysis is given in [53]. The procedure for chromatographic separation of Fe using an AG MP-1 anion exchange resin (100–200 mesh) followed that previously used by [54]. Following chromatographic separation, Fe isotope ratios were measured in high mass resolution mode on a Nu Plasma HR MC-ICP-MS using a standard-sample bracketing (SSB) approach. The Fe isotope results are expressed as deviations of the sample Fe isotope ratio from that of the reference material IRMM-14 in per mil:

$$\delta^{56}\text{Fe}_{\text{IRMM-014}} (\text{‰}) = [({}^{56}\text{Fe}/{}^{54}\text{Fe})_{\text{sample}}/({}^{56}\text{Fe}/{}^{54}\text{Fe})_{\text{IRMM-014}} - 1] \times 1000$$

$$\delta^{57}\text{Fe}_{\text{IRMM-014}} (\text{‰}) = [({}^{57}\text{Fe}/{}^{54}\text{Fe})_{\text{sample}}/({}^{57}\text{Fe}/{}^{54}\text{Fe})_{\text{IRMM-014}} - 1] \times 1000$$

The long-term external reproducibility is estimated to be better than 0.05‰ for $\delta^{56}\text{Fe}$ at the SD level, based on repeated measurements of in-house CAGS Fe solutions and national basaltic standard reference material CAGSR-1 (GBW-07105) against IRMM-014 [53].

Total inorganic carbon (TIC), total organic carbon (TOC), and the isotopic composition of organic carbon ($\delta^{13}\text{C}_{\text{org}}$) were measured on 10 selected samples at ALS Chemex, China. Abundances of TIC were analyzed with an Ethanolamine Color Coulomb Instrument after being treated with HClO_4 . The precision of the analyses (1σ) was better than 0.2%. Aliquots (200 mg) for TOC analysis were first treated with 10 vol.% HCl at 60 °C to remove carbonate [9], and then washed with distilled water to remove HCl. Afterward, the samples were dried overnight (50 °C) and then analyzed using an LECO CS-400 analyzer. Sample splits (300 mg to 1.5 g) for $\delta^{13}\text{C}_{\text{org}}$ analysis were acidified with 6 N HCl in a centrifuge beaker to remove any carbonates. The decalcified samples (30–100 mg) + CuO wire (1 g) were added to quartz tubes, and combusted at 500 °C for 1 h and at 850 °C for another 3 h. Isotopic ratios were analyzed using cryogenically purified CO_2 on a Finnigan MAT-253 mass spectrometer and are reported in standard δ -notation relative to the Vienna Pee Dee Belemnite (VPDB) standard:

$$\delta^{13}\text{C}_{\text{VPDB}} (\text{‰}) = [({}^{13}\text{C}/{}^{12}\text{C})_{\text{sample}}/({}^{13}\text{C}/{}^{12}\text{C})_{\text{VPDB}} - 1] \times 1000$$

Analytical precision for the values is better than $\pm 0.06\text{‰}$ (1σ) based on measurements of geostandards GBW04407 (−22.43‰) and IAEA-600 (−27.5‰).

4. Results

4.1. Occurrence and Microscopic Features of Siderite

The carbonate facies, which is mainly interbedded with mica-quartz schist and chlorite-quartz schist (Figure 3a), appears brown to yellow in exposed surfaces due to strong weathering (Figure 3d). There are many rotational porphyroblasts (Figure 3c) and fractures (Figure 3d). Fresh samples from deeper in the outcrop show alternating buff-white and black microbands with gradational contacts (Figure 3b,e), comprising siderite, quartz, and magnetite in varying proportions. The buff-white siderite-rich microbands (Figure 4a) are mainly composed of fine-grained siderite (10–60 μm), quartz (30–100 μm), and microcrystalline magnetite (10–30 μm), accounting for 30, 50, and 20 vol.%, respectively. As shown in BSE images, siderite grains are subhedral to anhedral, with some being replaced by magnetite at the edge (Figure 4b). In the center of siderite grains, micrometer-scale magnetite is also commonly observed as inclusions (Figure 4c). The black microbands contain mainly subhedral-anhedral magnetite grains (10–100 μm, ~60 vol.%) and siderite aggregations

(30–100 μm , ~20 vol.%), along with some tabular Fe-rich chamosite (50–150 μm) and quartz (Figure 4d). The siderite aggregations appear to be khaki and dirty, by which they can be distinguished from quartz that appears clear (Figure 4e). Clay minerals surrounding siderite grains are mainly chamosite in the form of green platy crystals (Figure 4e). Magnetite inclusions are also observed in some chamosite grains (Figure 4f). It is noted that fine-grained graphite (20–80 μm) is observed in the carbonate facies (Figure 4g,h), which is intergrown with the magnetite, calcite (10–50 μm), and apatite (10–20 μm) in some places (Figure 4i).

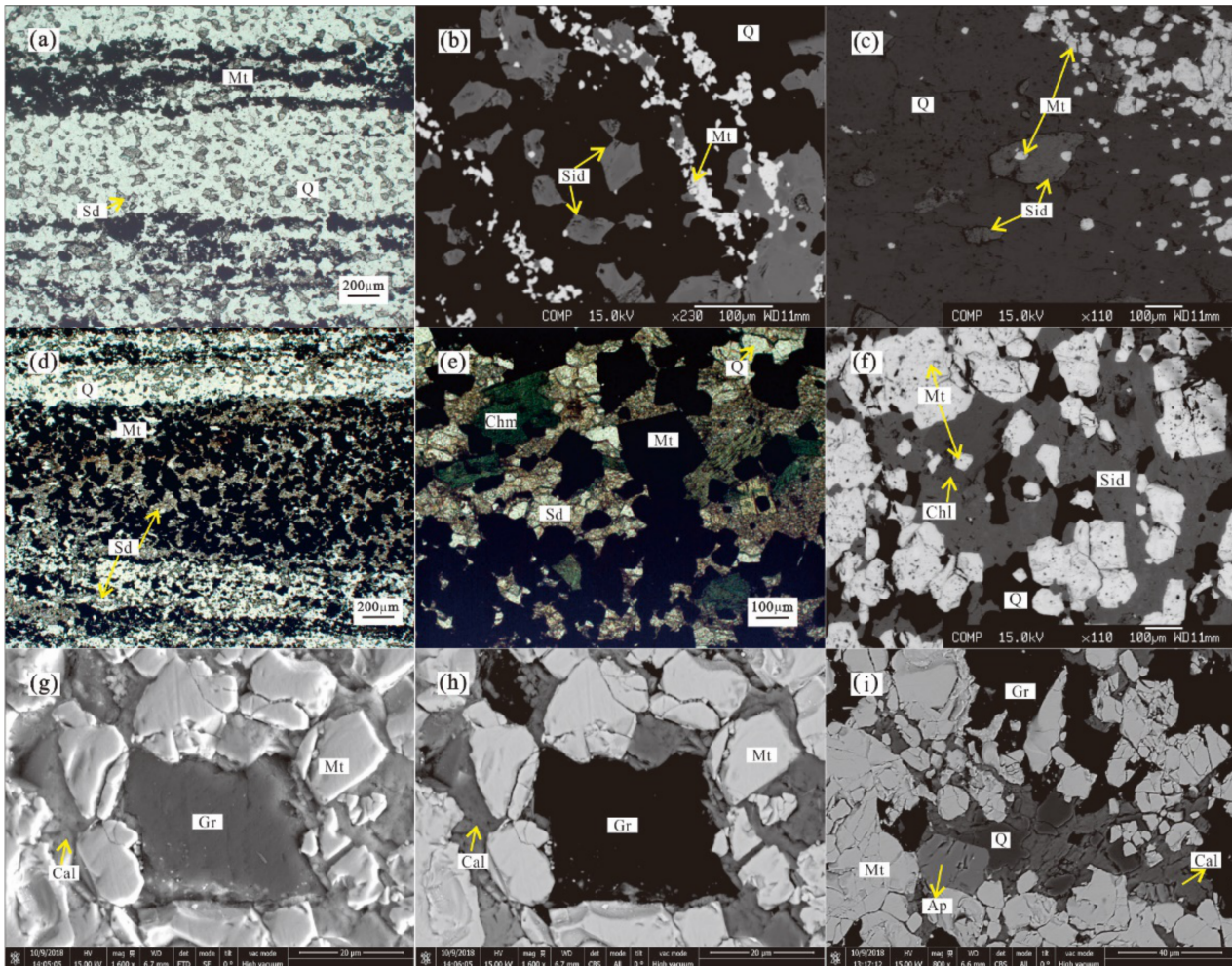


Figure 4. Photomicrographs showing representative textures of siderite in the carbonate facies BIF. (a) The buff-white microbands are composed mainly of fine-grained siderite (Sd) and quartz (plain-polarized light) (Q). (b) Siderite is subhedral to anhedral and replaced by magnetite (Mt) in part (scanning electron microscope image, SEM). (c) Micronmeter-sized granulous magnetites are found in the center of some siderite grains (SEM). (d) The black bands, comprising mainly subhedral-anhedral magnetite with some siderite aggregations (plain-polarized light). (e) The siderite aggregations appear to be khaki and dirty distinguishing them from quartz. There are also some green platy crystals of chamosite (Chm) (plain-polarized light). (f) The chamosite often encloses fine-grained magnetite (SEM). (g,h) Platy graphite (Gr, ~20 μm) in the carbonate facies (secondary electron image (SE) and back-scattered electron image (BSE) SEM, respectively). (i) Fine-grained graphite sometimes appears intergrown with the magnetite, calcite (Cal), and apatite (Ap) (SEM).

The major element compositions of Fe-rich carbonates are presented in Table 1 and plotted in Figure 5. Subhedral to anhedral siderite grains in the carbonate facies contain 47.48–55.31 wt.% FeO and 2.36–5.22 wt.% MgO with little CaO (<1 wt.%), corresponding to 87–93 mol.% and 6–12 mol.% of FeCO₃ and MgCO₃, respectively. The content of MnO is relatively low, ranging from 0.27 to 1.55 wt.%.

Table 1. EPMA data of iron-rich carbonate from the Dagushan BIF.

Composition	Unit	1	2	3	4	5	6	7	8	9	10	11	12	13	14
Na ₂ O	wt.%	0.06	0.07	0.00	0.10	0.09	0.05	0.08	0.04	0.01	0.03	0.10	0.07	0.02	0.06
MgO	wt.%	3.59	2.70	3.69	4.78	2.36	5.22	3.43	3.24	2.58	4.19	3.66	2.65	4.13	3.77
Al ₂ O ₃	wt.%	0.04	0.00	0.00	0.01	0.02	0.00	0.00	0.03	0.01	0.05	0.02	0.00	0.01	0.00
K ₂ O	wt.%	0.00	0.00	0.00	0.02	0.01	0.00	0.00	0.00	0.02	0.04	0.00	0.00	0.01	0.00
CaO	wt.%	0.66	0.64	0.69	0.49	0.29	0.32	0.85	0.56	0.72	0.42	0.77	0.61	0.11	0.20
FeO	wt.%	49.78	51.88	50.18	48.99	50.13	47.67	49.15	48.54	55.31	50.10	47.48	52.85	53.57	49.02
MnO	wt.%	1.19	1.08	1.35	1.14	0.81	1.26	1.27	1.55	0.92	1.42	1.67	1.22	0.54	0.27
TiO ₂	wt.%	0.00	0.01	0.03	0.00	0.02	0.00	0.03	0.00	0.01	0.04	0.02	0.00	0.01	0.00
SiO ₂	wt.%	0.01	0.05	0.06	0.00	0.03	0.02	0.00	0.06	0.01	0.03	0.02	0.05	0.01	0.01
Cr ₂ O ₃	wt.%	0.02	0.03	0.00	0.01	0.00	0.01	0.00	0.02	0.00	0.00	0.01	0.02	0.00	0.00
NiO	wt.%	0.01	0.04	0.02	0.00	0.01	0.00	0.00	0.01	0.00	0.01	0.02	0.01	0.01	0.00
FeCO ₃	%	90.19	92.47	90.01	87.85	93.65	86.94	90.08	90.93	93.00	89.42	89.41	92.75	90.68	90.52
CaCO ₃	%	1.33	1.26	1.38	0.97	0.60	0.65	1.73	1.16	1.34	0.83	1.61	1.19	0.21	0.41
MgCO ₃	%	8.48	6.27	8.62	11.17	5.75	12.41	8.19	7.91	5.65	9.75	8.98	6.06	9.11	9.07

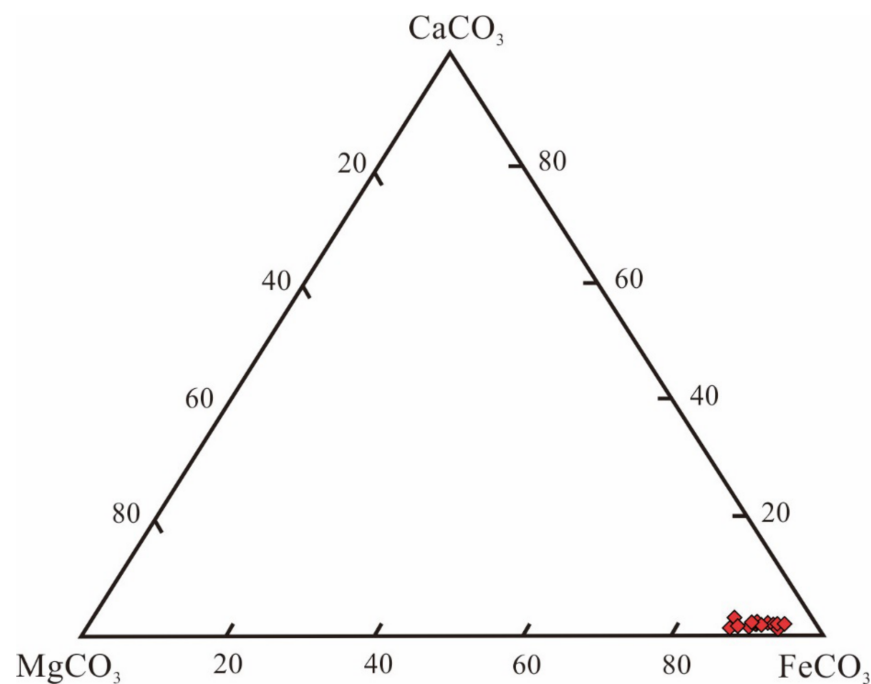


Figure 5. Major mineral end-member compositions of individual siderite in the Dagushan carbonate facies BIF based on the modal proportion of carbonate minerals. Three end-members are siderite, calcite, and dolomite, respectively. Data was obtained by electron microprobe analysis.

4.2. Bulk Carbon Content and Isotopes and Siderite Iron Isotopes

The TOC and TIC of the BIF samples, and carbon isotope ratios of C_{org}, are presented along with previously published siderite C isotope data ($\delta^{13}\text{C}_{\text{Sid}}$) in Table 2. The TOC contents in BIF samples are less than 0.11 wt.%, consistent with the minor amount of C_{org} (graphite) observed microscopically, while the TIC contents of the samples are higher and range widely from 0.92 to 3.36 wt.%. Carbon isotope ratios of $\delta^{13}\text{C}_{\text{org}}$ are relatively consistent, varying from -26.8‰ to -23.2‰ , with an average of -25.4‰ . There is no obvious correlation between TOC and $\delta^{13}\text{C}_{\text{org}}$ in the dataset. Neither is any obvious correlation observed between $\delta^{13}\text{C}_{\text{Sid}}$ and $\delta^{18}\text{O}_{\text{Sid}}$ values (Figure S1), suggesting that samples have only undergone low-grade alteration [55]. In addition, the contents of primary organic carbon precipitated on the seafloor are relatively low, varying from 0.73 to 1.25 wt.%, and the calculation process is shown in Table 3.

Table 2. Carbonate and organic carbon geochemical data of the Dagushan BIF.

Sample	TOC	TIC	$\delta^{13}\text{C}_{\text{org}}$	$\delta^{13}\text{C}_{\text{carb}}^1$	$\delta^{18}\text{O}_{\text{carb}}^1$	DIC _{org}	%DIC _{org} /TIC
Unit	wt. %	wt. %	‰, VPDB	‰, VPDB	‰, SMOW	wt. %	%
D-3-1	0.08	2.98	−26.50	−3.53	12.41	0.40	13.32
D-3-2	0.05	2.57	−26.80	−4.64	13.87	0.44	17.31
D-3-3	0.06	0.92	−24.80	−3.85	11.02	0.14	15.52
D-3-4	0.05	1.81	−24.44	−4.12	12.94	0.31	16.86
D-3-5	0.06	2.19	−25.32	−4.89	13.63	0.42	19.31
D-4-1	0.04	1.48	−24.90	−6.20	11.93	0.37	24.90
D-4-2	0.11	2.41	−23.15	−1.57	13.31	0.16	6.78
D-4-3	0.07	2.54	−26.33	−5.34	12.71	0.52	20.28
D-4-4	0.09	1.85	−26.74	−2.90	12.18	0.20	10.85
D-4-5	0.08	3.36	−25.01	−3.68	13.92	0.49	14.71
average	0.07	2.21	−25.40	−4.07	12.79	0.35	15.98

¹ The $\delta^{13}\text{C}_{\text{carb}}$ and $\delta^{18}\text{O}_{\text{carb}}$ data are from [56]. TOC = the content of total organic carbon in samples; TIC = the content of total inorganic carbon; $\delta^{13}\text{C}_{\text{org}}$ = carbon isotope of organic carbon; [DIC]_{org} = inorganic carbon derived from remineralized organic carbon; % [DIC]_{org}/TIC = percentage of remineralized organic carbon in total inorganic carbon (with TIC = [DIC]_{org} + [DIC]_{sw}).

Table 3. Calculation of the organic carbon.

Sample	m_c	m_{Fe}	M_{Sid}	Total Fe_2O_3^1	TFe	M_{Mt}	$M_{\text{Fe(II)-Mt}}$	$M_{\text{TFe(II)}}$	$m_{\text{Fe(II)}}$	M_{oc}	TOC*	Consumed TOC (%)
D-3-1	0.25	0.25	13.91	48.79	34.15	20.25	6.75	20.66	0.37	1.11	1.19	93.26
D-3-2	0.21	0.21	11.99	50.86	35.60	23.61	7.87	19.86	0.35	1.06	1.11	95.51
D-3-3	0.08	0.08	4.29	41.04	28.73	24.43	8.14	12.44	0.22	0.67	0.73	91.74
D-3-4	0.15	0.15	8.45	53.80	37.66	29.21	9.74	18.18	0.32	0.97	1.02	95.12
D-3-5	0.18	0.18	10.22	50.74	35.52	25.30	8.43	18.65	0.33	1.00	1.06	94.34
D-4-1	0.12	0.12	6.91	47.46	33.22	26.32	8.77	15.68	0.28	0.84	0.88	95.45
D-4-2	0.20	0.20	11.25	58.79	41.15	29.91	9.97	21.22	0.38	1.14	1.25	91.18
D-4-3	0.21	0.21	11.85	59.60	41.72	29.87	9.96	21.81	0.39	1.17	1.24	94.35
D-4-4	0.15	0.15	8.63	35.23	24.66	16.03	5.34	13.98	0.25	0.75	0.84	89.27
D-4-5	0.28	0.28	15.68	46.88	32.82	17.14	5.71	21.39	0.38	1.15	1.23	93.47

¹ Total Fe_2O_3 data are from [56]. m_c = molar abundance of carbon ($m_c = \text{TIC}/12 \text{ g/mol}$); m_{Fe} = molar abundance of iron ($m_{\text{Fe}} = m_c$); M_{Sid} = mass fraction of Fe in siderite ($M_{\text{Sid}} = m_{\text{Fe}} * 56 \text{ g/mol} = \text{TIC}/12 \text{ g/mol} * 56 \text{ g/mol}$); TFe = Total Fe content of the samples; M_{Mt} = Total Fe content in magnetite ($M_{\text{Mt}} = \text{TFe} - M_{\text{Sid}}$); $M_{\text{Fe(II)-Mt}}$ = Fe(II) content in magnetite ($M_{\text{Fe(II)-Mt}} = M_{\text{Mt}}/3$); $M_{\text{TFe(II)}}$ = Total Fe(II) content in samples ($M_{\text{TFe(II)}} = M_{\text{Fe(II)-Mt}} + M_{\text{Sid}}$); $m_{\text{Fe(II)}}$ = molar abundance of total Fe(II) ($m_{\text{Fe(II)}} = (M_{\text{Fe(II)-Mt}} + M_{\text{Sid}})/56 \text{ g/mol}$); M_{oc} = mass fraction of required organic carbon content ($M_{\text{oc}} = m_{\text{TFe(II)}}/4 * 12 \text{ g/mol}$); TOC* = minimum total organic carbon that precipitated on the seafloor ($\text{TOC}^* = M_{\text{oc}} + \text{TOC}$).

The iron isotope compositions ($\delta^{56}\text{Fe}$) of siderite from the Dagushan BIF are predominantly positive and range from -0.180 to $+0.463\text{‰}$, with a mean value of $+0.187\text{‰}$, and show an entirely mass-dependent relationship with $\delta^{57}\text{Fe}$ ($R^2 = 0.99$) (Table 4, Figure S2). Only three samples have slightly negative $\delta^{56}\text{Fe}$ values between -0.18 and -0.06‰ . Analytical error on the sample measurements (1 standard deviation) varies from 0.011 to 0.052.

Table 4. Iron isotope data of siderite from the Dagushan BIF.

Sample	$\delta^{57/54}\text{Fe}$	SD	$\delta^{56/54}\text{Fe}$	SD
D-3-1	0.618	0.019	0.390	0.040
D-3-2	-0.119	0.049	-0.063	0.042
D-3-3	0.446	0.030	0.316	0.013
D-3-4	0.284	0.006	0.181	0.015
D-3-5	-0.260	0.024	-0.180	0.022
D-4-1	-0.205	0.043	-0.129	0.033
D-4-2	0.636	0.031	0.463	0.043
D-4-3	0.149	0.052	0.091	0.011
D-4-4	0.680	0.014	0.438	0.052
D-4-5	0.545	0.058	0.367	0.049
Average	0.277	0.032	0.187	0.032

5. Discussion

5.1. Mineral Paragenesis

Siderite, typically occurring as microcrystalline, single rhomb-shaped crystals or massive layers, is the most common carbonate mineral in BIFs, and it may form penecontemporaneously with early ferric oxyhydroxide precipitates or during later diagenesis [13,16,17,57,58]. Siderite and magnetite are the main Fe-bearing minerals in the Dagushan carbonate facies BIF.

Fine-grained subhedral siderite crystallites ($<50\ \mu\text{m}$) and fine-grained magnetite ($<50\ \mu\text{m}$) are evenly distributed amongst the quartz (Figure 4a). These are likely to have formed relatively rapidly during the early stage of diagenesis due to their small sizes. Moreover, fine-grained magnetite occurs as inclusions within some medium to large-grained subhedral-euhedral siderites ($50\text{--}150\ \mu\text{m}$) (Figure 4c), whereas siderite is not found within magnetite grains, suggesting that large-grained siderite post-dates the fine-grained magnetite and probably formed later during diagenesis. Additionally, the irregular siderite aggregates in the iron-rich microbands, intergrown with green platy chamosite (Figure 4e) and medium to large coarse-grained magnetite ($50\text{--}150\ \mu\text{m}$), are formed from preferentially concentrated siderite grains where several Fe oxide layers coalesce due to burial compaction, and may distort the primary microlamination (Figures 3c and 4d), providing further evidence for siderite formation during later diagenesis. In addition, medium to large-grained siderite grains are occasionally replaced by magnetite on the edges (Figure 4b), likely through metamorphic alteration and oxidation.

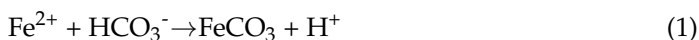
In sum, fine-grained magnetite and siderite are likely to have formed during the early diagenesis, while medium to large-grained magnetite, siderite aggregates possibly formed during later diagenesis. Finally, siderite may have been oxidized to magnetite during subsequent metamorphism.

5.2. Formation Pathways of Siderite

5.2.1. Direct Precipitation from Seawater

Siderite is typically formed in anoxic and Fe-rich (but S-poor) conditions under high alkalinity [10–12,59]. Accordingly, some previous publications have argued that, similar to other marine carbonates, ancient siderite in BIF formed through the combination of dis-

solved Fe(II) with dissolved carbon dioxide, in the form of HCO_3^- , and directly precipitated from seawater via the following reaction [13,20–22,24,25,60]:



Although it has recently been argued that the kinetics of Fe(II)-carbonate precipitation in Precambrian seawater would have limited its direct precipitation [26]. When considering the direct precipitation from seawater, the $\delta^{13}\text{C}_{\text{Sid}}$ composition can be used to evaluate whether siderite precipitated directly in equilibrium with seawater. The dissolved inorganic carbon (DIC) pool in Precambrian seawater is expected to have had $\delta^{13}\text{C}$ values close to 0‰, except for some anomalous periods in the early Paleoproterozoic and the late Neoproterozoic [61]. Thus, carbonate minerals comprising limestones and dolomite precipitated directly from the seawater, and typically have $\delta^{13}\text{C}_{\text{carb}}$ values of ~0‰ [61,62]. For example, Ca-Mg carbonates associated with the 2.52 Ga Gamoha Formation BIFs [63–66] and stratigraphically equivalent Campbellrand platform rocks [67] have $\delta^{13}\text{C}_{\text{carb}}$ values from –1.0 to 0‰. Given that C isotope fractionation between calcite and siderite in equilibrium with the same fluid at 25 °C is about –0.5‰ [68], estimated values of $\delta^{13}\text{C}_{\text{Sid}}$ formed in equilibrium with Archean seawater should range from –1.5 to –0.5‰. However, the distinctly negative $\delta^{13}\text{C}_{\text{Sid}}$ values, ranging from –6.20 to –1.57‰, in the Dagushan BIF (Table 2) fall below the expected values for seawater-derived siderite, suggesting that the more negative $\delta^{13}\text{C}_{\text{Sid}}$ values indicate that an additional negative C isotope reservoir, such as organic matter, must have contributed to siderite formation (see next section).

The Fe isotopic signatures in Dagushan siderites corroborate the C isotopes. The main Fe(II) source of the Archean ocean are hydrothermal fluids [4] which are expected to have a $\delta^{56}\text{Fe}$ composition of around –0.2‰ or less [29,31]. In addition, the equilibrium Fe(II)aq-siderite fractionation factor is estimated to be $-0.5 \pm 0.2\text{‰}$ from experimental observations [69], or –2.1 to –1.6‰ based on theoretical calculations [70–72]. Accordingly, siderites precipitated in equilibrium with seawater are predicted to have negative Fe isotopic ratios from –2 to –0.5‰. Similar light $\delta^{56}\text{Fe}$ values are observed in Fe-poor carbonates from the Wittenoom Dolomite in the Hamersley basin [31]. By contrast, siderites in the Dagushan BIF have $\delta^{56}\text{Fe}$ values that range from –0.180 to +0.463‰, uniformly higher than values predicted for seawater-precipitated siderite. In sum, siderites from our study area do not carry typical isotopic signatures reflective of formation in equilibrium with seawater. Therefore, we posit that siderite in the Dagushan BIF could not have precipitated directly in the water column.

5.2.2. Authigenic Precipitation from Porewater by DIR

Another proposed formation pathway for siderite in BIFs is authigenic precipitation from sediment porewater, facilitated by dissimilatory iron reduction (DIR). DIR is a widespread microbial metabolic pathway through which Fe(III)-reducing bacteria oxidize organic carbon for energy and tie electron transport to the reduction of an Fe(III)-oxyhydroxide, such as ferrihydrite ($\text{Fe}(\text{OH})_3$). This anaerobic metabolism produces dissolved Fe(II), depending on the porewater composition, can facilitate the precipitation secondary Fe(II)-bearing minerals such as siderite (R.2). This biologically induced form of biomineralization has been demonstrated to be a viable pathway capable of accounting for siderite in both modern sediments [73,74] and the rock record [28,29,32,33,75,76].



A flux of reactive ferrihydrite and C_{org} to the seafloor in Neoproterozoic oceans, where dissimilatory sulfate reduction was suppressed by low sulfate levels, would support high levels of DIR [29]. Such a pathway could have converted ferrihydrite to siderite in the Dagushan BIF, as is supported by several lines of evidence including petrographic observations, negative $\delta^{13}\text{C}_{\text{Sid}}$ values, and varying $\delta^{56}\text{Fe}$ values in siderites, while the presence of graphite supports the previous presence of organic biomass that could have

acted as the electron donor to facilitate DIR. In this regard, the fine-grained graphite (~20 μm , Figure 4g,h) is likely to be the final product of remnant organic carbon after being metamorphosed.

From a petrographic perspective, there is no siderite found in magnetite grains, whereas small magnetite grains occur as inclusions within siderite (Figure 4c). This is important because not only does it confirm a diagenetic pathway rather than precipitation from seawater, but it also implies that magnetite formed even earlier. Furthermore, some siderite and quartz grains appear as irregular aggregates that have distorted the primary microlamination and several Fe-rich microbands (Figure 3c), suggesting that these were preferentially concentrated during burial compaction.

The negative $\delta^{13}\text{C}_{\text{Sid}}$ values, ~ -6.20 to -1.57% , of the Dagushan BIFs, which are significantly lower than those expected via precipitation from seawater, require a source of C with a lighter isotopic composition. The best candidate for this is the organic matter present in the Dagushan BIFs which displays a narrow range of very low $\delta^{13}\text{C}_{\text{Org}}$ between -26.8 and -23.2% . The oxidation of C_{Org} delivers isotopically light dissolved inorganic carbon (DIC) to porewaters, where it mixes with seawater-derived DIC with $\delta^{13}\text{C}$ around 0% ($[\text{DIC}]_{\text{sw}}$). Theoretically, siderites with $\delta^{13}\text{C}$ ratios nearing -25% could be formed entirely from a pool of carbonate derived through DIR, while siderites possessing $\delta^{13}\text{C}$ ratios around 0% could have formed entirely from an inorganic reservoir derived from seawater. Accordingly, the wide range of negative $\delta^{13}\text{C}_{\text{Sid}}$ values in the Dagushan BIF may reflect varying proportions of both end member sources (i.e., seawater/diagenetic HCO_3^- anions) during siderite formation within sediments.

Mixing of bicarbonate pools is further implied by a positive correlation ($R = 0.86$, Figure 6) between TOC and $\delta^{13}\text{C}_{\text{Sid}}$. If the TOC contents of primary sediments were initially similar, this positive correlation would indicate that in samples where the residual organic matter content is lower, a relatively larger fraction of the organic matter was oxidized through DIR and a higher proportion of DIR-derived C participated in the forming of siderite, leading to a lower carbon isotope value.

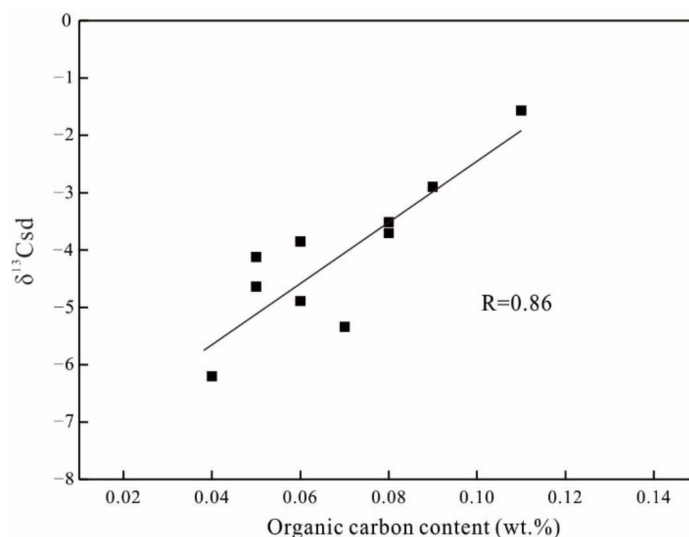


Figure 6. Correlation diagram for organic carbon content (TOC, wt.%) of the bulk rock and carbon isotope composition of the siderite ($\delta^{13}\text{C}_{\text{Sid}}$, ‰).

Through a simple mass-balance model (R.3) presented in [3], the proportions of HCO_3^- ($\delta^{13}\text{C}_{\text{sw}} = 0\%$) from seawater and organic carbon ($\delta^{13}\text{C}_{\text{Org}} = -25\%$) may be calculated as follows:

$$[\text{DIC}]_{\text{Sid}} \delta^{13}\text{C}_{\text{Sid}} = [\text{DIC}]_{\text{Org}} \delta^{13}\text{C}_{\text{Org}} + [\text{DIC}]_{\text{sw}} \delta^{13}\text{C}_{\text{sw}} \quad (3)$$

where $[\text{DIC}]_{\text{Sid}}$ and $[\text{DIC}]_{\text{sw}}$ are the mass fractions of inorganic C in siderite and seawater, respectively, while $[\text{DIC}]_{\text{Org}}$ represents inorganic carbon content that is derived from organic

carbon though DIR. The $\delta^{13}\text{C}_{\text{Sid}}$, $\delta^{13}\text{C}_{\text{org}}$, and $\delta^{13}\text{C}_{\text{sw}}$ are the carbon isotope compositions of siderite (~ -6.20 to -1.57‰), organic carbon (~ -26.80 to -23.2‰), and seawater ($\sim 0\text{‰}$), respectively. Accordingly, the proportion of the organic carbon that contributed to siderite formation ($[\text{DIC}]_{\text{org}}/\text{TIC}$) depends on the value of $\delta^{13}\text{C}_{\text{org}}/\delta^{13}\text{C}_{\text{Sid}}$, and corresponds to about 6.78–24.90% of DIR-derived C in Dagushan BIF siderites (Table 2).

In addition to C isotopes, the Fe isotope composition of Fe-rich carbonates can be used to probe their formation processes. As mentioned above, siderites in the Dagushan BIF have $\delta^{56}\text{Fe}$ values from -0.180 to $+0.463\text{‰}$, which is best explained through inheritance from a ferrihydrite precursor formed through the partial oxidation of dissolved Fe(II) that typically produces $\delta^{56}\text{Fe}$ fractionations of $\sim +1.2\text{‰}$ [77]. This was then followed by DIR (pathway 2, Figure 7), rather than direct precipitation from seawater, or conversion from green rust [34], as these would result in negative fractionations (pathway 1, Figure 7). The DIR in the Dagushan BIF was likely not quantitative, since magnetite formed during diagenesis is commonly present in the carbonate facies. If so, significant $\delta^{56}\text{Fe}$ fractionations would have accompanied DIR, since equilibrium fractionation between produced Fe(II) and the ferrihydrite surface is around -3.0 to -0.5‰ [16,29,78–80]. Assuming $\Delta\text{Fe}_{\text{Fe(II)-Fe(OH)3}} = -2\text{‰}$ and a 50% degree of reduction under equilibrium conditions, then the microbially reduced Fe(II) and the remaining ferrihydrite would have had a $\delta^{56}\text{Fe}$ value of $\sim -0.5\text{‰}$ and $+1.5\text{‰}$, respectively, if calculated from simple mass balance with $\delta^{56}\text{Fe}_{\text{Fe(OH)3}} \sim +0.5\text{‰}$. Furthermore, as is suggested to be the case with DIC, Fe(II) with low- $\delta^{56}\text{Fe}$ could have been mobilized in the sediment pores, and mixed with Fe(II) from the seawater which had a $\delta^{56}\text{Fe}$ value of around 0‰ , or higher in the Neoproterozoic [81,82].

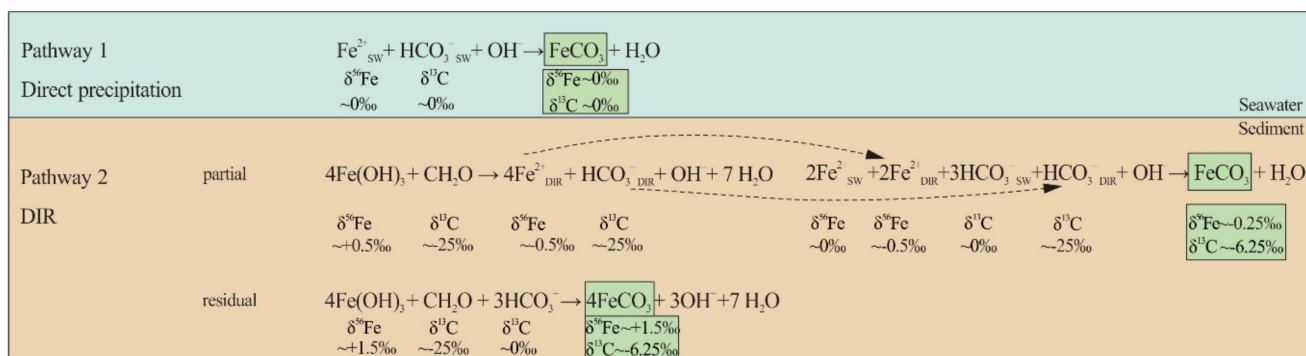


Figure 7. Schematic diagram for the diagenetic origin of siderite in the Dagushan BIF based on mineralogical, chemical, and C and Fe isotope data, modified from [16].

The precise iron isotope value is dependent on the proportions of Fe(II) from the DIR and seawater inputs. For example, if the ratio is 1:1, siderite would be expected to have a $\delta^{56}\text{Fe}$ composition of -0.25‰ (pathway 2, partial reaction, Figure 7). By contrast, siderite formed from the remnant substrate by near-complete reduction of residual ferrihydrite would inherit a positive $\delta^{56}\text{Fe}$ signature, and is expected to have $\delta^{56}\text{Fe}$ values around $+1.5\text{‰}$ (pathway 2, residual reaction), but this greatly depends upon the initial value of ferrihydrite, the amount of Fe(II) that was converted into magnetite, and the prior loss of low- $\delta^{56}\text{Fe}$ Fe(II) into the water column. The Fe isotope values of siderites in the Dagushan BIF are consistent with those predicted above. These features are also similar to the siderites in the Brockman Iron Formation (Hamersley Basin, Western Australia), the Kuruman Iron Formation (Transvaal Supergroup, South Africa), and the Cauê Formation BIF (Brazil) [16,29,31,76], which is a strong indicator that DIR played a significant role in the origin of siderite in many Neoproterozoic to Paleoproterozoic BIFs.

5.3. Calculation for the Contents of Organic Carbon Precipitated on the Seafloor

Combining the content of residual TOC with the total iron content of the samples in the Dagushan BIF, the total primary organic carbon content precipitated on the seafloor

with the BIF (TOC*) may be approximated, ranging from 0.73 to 1.25 wt.% (Table 3). Assuming that all the total inorganic carbon (TIC) is from siderite, we can then estimate the molar abundance of carbon (m_c) in siderite: $m_c = \text{TIC}/12 \text{ g/mol}$, which would equal the mole number of the iron atom (m_{Fe}) in siderite based on the stoichiometric formula for siderite, FeCO_3 . Accordingly, the mass fraction of Fe in siderite (M_{Sid}) is: $M_{\text{Sid}} = m_{\text{Fe}} * 56 \text{ g/mol} = m_c * 56 \text{ g/mol} = \text{TIC}/12 \text{ g/mol} * 56 \text{ g/mol}$. If we consider that the total Fe (TFe) represents the contribution from siderite and magnetite and ignore the Fe contributed from chamosite, due to its low modal content, we then calculate the Fe contributed by magnetite (M_{Mt}): $M_{\text{Mt}} = \text{TFe} - M_{\text{Sid}}$. Magnetite (Fe_3O_4) has 1/3 Fe(II) and 2/3 Fe(III), which means that the Fe(II) content in magnetite ($M_{\text{Fe(II)-Mt}}$) can be calculated as: $M_{\text{Fe(II)-Mt}} = M_{\text{Mt}}/3$. Consequently, total Fe(II) content $M_{\text{TFe(II)}}$ is the sum of $M_{\text{Fe(II)-Mt}}$ and M_{Sid} , and mole number is $=M_{\text{Fe(II)-Mt}} + M_{\text{Sid}}/56 \text{ g/mol}$. During Fe(III) reduction, a ratio of 1C:4Fe(III) ratio is required if organic carbon serves as the reductant for chemoheterotrophic metabolism [R.4] [28], and thus, the required organic carbon content is: $M_{\text{oc}} = m_{\text{TFe(II)}}/4 * 12 \text{ g/mol}$.



Therefore, the minimum total organic carbon that precipitated on the seafloor during BIF deposition may be estimated by combining M_{oc} and tested residual TOC in samples. It is noted here that graphite is sparsely distributed within our samples, and that overall the TOC preserved in our samples remains low (down to 0.04 wt.%). This is much lower than those of other BIFs such as the Mozaan Group, South Africa, which have TOC contents ranging from 0.4 to 2.5 wt.% [83].

Constant organic material inputs to oceans are usually in the form of allochthonous and/or autochthonous particulates that sink from the surface down onto the seafloor. The water depth and the distance from the shore are the predominant factors that govern the flux of organic material to the seafloor [84]. According to Chester [85], less than 0.1% of organic material makes its way through deeper waters without being remineralized and ends up buried into pelagic sediments, compared to 5% in nearshore sediments. This relationship may help to explain the relatively low C_{org} abundance in the study materials, as the Dagushan BIFs were likely deposited in bathyal-abysmal basin.

5.4. Comparison with Siderites in Other BIFs through Time

Iron and C isotope data of siderite samples from a selection of BIFs of different ages (from 3.8 to 1.3 Ga) are summarized in Table 5 and plotted in Figure 8. These include the ~3.8 Ga Isua BIFs, West Greenland [31,86], the ~2.65 Ga Cauê BIF, Brazil [76], the ~2.45 Ga Kuruman BIFs, South Africa [16], the ~1.3 Ga Jingtieshan BIF, China [87], and the ~2.52 Ga Dagushan BIF, China (this study).

Most of the siderite samples summarized here range between -8 to -3‰ in $\delta^{13}\text{C}$ and -0.75 to $+0.75\text{‰}$ in $\delta^{56}\text{Fe}$. Only a few samples are close to the estimated value of Archean seawater-derived siderite (Figure 8), which implies that siderites in BIF are generally not formed in equilibrium with seawater, but instead are products of early diagenetic mineral formation in the soft sediment prior to lithification [16,76]. One exception is the Jingtieshan BIF, which has a narrower Fe isotope range between -0.71‰ and -0.41‰ (apart from a single sample with $\delta^{56}\text{Fe} = -1.62\text{‰}$), suggesting the possibility of isotope equilibrium with submarine hydrothermal fluids and seawater [81]; however, even there the $\delta^{13}\text{C}$ values imply a significant contribution from remineralized C_{org} . The $\delta^{56}\text{Fe}$ and $\delta^{13}\text{C}$ signatures of siderite in the ~3.8 Ga Isua and 2.65 Ga Cauê BIFs—similarly an Algoma-type BIF—are the most similar to those of the Dagushan BIF. The most significant difference is that all $\delta^{56}\text{Fe}$ values of siderite in the Isua BIF samples are positive, which have been interpreted as a result of complete DIR [31]. Thus, despite the large age difference between different siderites at different locations, microbial DIR seems to have persisted as a dominant influence on sediment geochemistry from ~3.8 to ~2.45 Ga in BIF depositional settings [31,39,76].

Table 5. Statistical data of the iron and carbon isotopes of siderites through different time periods.

BIF Name	Loction	Formation Age (Ga)	Type ¹	¹³ C (‰)	⁵⁶ Fe(‰)	Origin	References
Isua BIF	Greenland	~3.8	A	−4.52~−5.94	+0.24~+0.76	DIR	[31,86]
Helen IF	Wawa, Ontario	~2.75	A	~0‰	-	Direct precipitation	[25]
Brockman IF	Hamersley, Australia	~2.5	S	−12.59~−7.45	−1.08~+1.21	DIR	[31,87]
Brockman IF	Hamersley, Australia	~2.5	S	−6.92~−11.00	-	Direct precipitation	[21]
Brockman IF	Hamersley, Australia	~2.5	S	-	−2.06~+1.00	DIR	[29]
Kuruman, Gamohaan BIFs	Transvaal, South Africa	~2.5	S	−2.6~−12	−0.32~+0.99	DIR	[16]
Cauê IF	Quadrilátero Ferrífero, Brazil	~2.45	S	-	−2.0~+1.33	DIR	[76]
Xiamaling Formation	Hebei, China	~1.40–1.35	-	−24.44~−12.35	-	DIR	[59]
Jingtieshan BIF	Gansu, China	~1.3	-	−8.4~−3.0	−0.42~−0.71	Direct precipitation	[88]

¹ Type “A” and “S” represent “Algoma” and “Superior”, respectively.

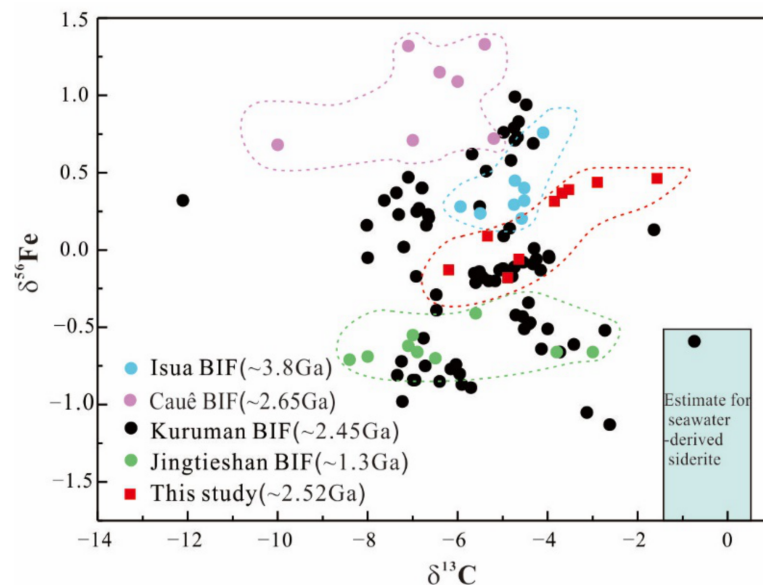


Figure 8. Iron ($\delta^{56}\text{Fe}$) and carbon ($\delta^{13}\text{C}$) isotope data for siderites from typical BIFs of different ages, including the ~3.8 Ga Isua BIFs (blue circles, [31,86]), ~2.45 Ga Kuruman BIFs, (black circles, [16]), ~2.65 Ga Cauê BIF (pink circles, [76]), ~1.3 Ga Jingtieshan BIFs (green circles, [88]), and ~2.52 Ga Dagushan BIF (red squares) in this study. The blue box is the predicted range of isotopic compositions for iron-rich carbonates precipitated directly from and in isotopic equilibrium with Archean seawater based on experimental [68,69] and theoretical estimates [70–72] of equilibrium isotope fractionation between $\text{Fe(II)}_{\text{aq}}$ -siderite and HCO_3^- -siderite.

6. Conclusions

Based on the Fe and C isotopic analyses presented here, the formation pathways for siderite in the carbonate facies of the ~2.52 Ga Dagushan BIF (Anshan area, China) are well constrained. The relatively negative $\delta^{13}\text{C}$ and highly variable $\delta^{56}\text{Fe}$ values are inconsistent with the siderites forming in equilibrium with Archean seawater and negate the potential for the direct precipitation from the water column in our study area. Thus, our siderite samples cannot be used as a direct proxy of paleomarine conditions, but instead they represent a valuable record of early diagenetic processes.

The significant pathway for siderite formation was likely DIR, where organic matter was oxidized with ferrihydrite acting as the terminal electron acceptor, and siderite being produced as a passive by-product. The positive and negative $\delta^{56}\text{Fe}$ values of siderites measured in this study may be explained, respectively, by partial to quantitative reduction of the precursor ferrihydrite, which was originally the product of partial oxidation which generated the positive $\delta^{56}\text{Fe}$ values. However, quantitative reduction would require that all ferrihydrite was reduced by DIR and all ferrihydrite was transformed to siderite. This is contradicted by abundant magnetite grains within the samples studied here. Consequently, a multiple-stage DIR process may offer the best explanation for siderite formation in the study area. Here, Fe(II) produced by partial reduction of the precursor ferrihydrite through DIR could have mixed with seawater-sourced Fe(II) in sediment porewater to produce a range of $\delta^{56}\text{Fe}$ values. By contrast, sustained reaction of residual ferrihydrite would have produced positive $\delta^{56}\text{Fe}$ values up to +1.5‰. The $\delta^{56}\text{Fe}$ of the precursor ferrihydrite, the degree of DIR, and the proportion of DIR-derived and seawater-sourced Fe(II) that contributed to siderite formation are the most significant factors influencing the $\delta^{56}\text{Fe}$ of siderites. In addition, the negative $\delta^{13}\text{C}$ values in the Dagushan BIF require both DIR-derived and seawater-sourced HCO_3^- , with less than 25% being derived through DIR, consistent with the overall low C_{org} content of the Dagushan BIF. Similarities in the C and Fe isotope systematics between the Dagushan BIF and a series of other Archean-Paleoproterozoic are a testament to the pervasive nature of DIR in Precambrian marine sediments.

Supplementary Materials: The following are available online at <https://www.mdpi.com/2075-163X/11/1/94/s1>, Figure S1: Correlation diagram of $\delta^{13}\text{C}_{\text{sid}}$ and $\delta^{18}\text{O}_{\text{sid}}$ values, Figure S2: A plot of $\delta^{57}\text{Fe}$ - $\delta^{56}\text{Fe}$ values showing an entirely mass-dependent ($R^2 = 0.99$).

Author Contributions: Conceptualization, X.T. and C.W.; methodology, C.W.; software, X.T.; validation, X.T. and C.W.; formal analysis, X.T.; investigation, X.T., Z.P., Q.W. and P.L.; resources, C.W.; data curation, X.T.; writing—original draft preparation, X.T.; writing—review and editing, Y.L., L.J.R., K.M., L.Z., M.Z., C.W., and K.O.K.; visualization, X.T.; supervision, C.W. and L.Z.; project administration, C.W.; funding acquisition, C.W. All authors have read and agreed to the published version of the manuscript.

Funding: This research was funded by the National Natural Science Foundation of China, grant number “41872087, 41890833, and 41902078” and the Key Research Program of the Institute of Geology and Geophysics, CAS, grant number “IGGCAS-201905”.

Institutional Review Board Statement: Not applicable.

Informed Consent Statement: Not applicable.

Data Availability Statement: Data is contained within the article.

Acknowledgments: We greatly appreciate the help of Dabo Xu, Banglu Zhang, and Jingbo Nan during field work. We are grateful to Zhihong Li for the help with laboratory analyses.

Conflicts of Interest: The authors note that L.J.R. was a guest editor for this special issue of Minerals; however, L.J.R. played no role in the editorial handling of this manuscript. The authors declare there is no other conflict of interest.

References

- James, H.L. Sedimentary facies of iron-formation. *Econ. Geol.* **1954**, *49*, 235–293. [[CrossRef](#)]
- Bekker, A.; Slack, J.F.; Planavsky, N.; Krapez, B.; Hofman, A.; Konhauser, K.O.; Rouxel, O.J. Iron formation: The sedimentary product of a complex interplay among mantle, tectonic oceanic, and biospheric processes. *Econ. Geol.* **2010**, *105*, 467–508. [[CrossRef](#)]
- Konhauser, K.O.; Planavsky, N.J.; Hardisty, D.S.; Robbins, L.J.; Warchola, T.J.; Haugaard, R.; Lalonde, S.V.; Partin, C.A.; Oonk, P.B.H.; Tsikos, H.; et al. Iron formations: A global record of Neoproterozoic to Palaeoproterozoic environmental history. *Earth Sci. Rev.* **2017**, *172*, 140–177. [[CrossRef](#)]
- Bau, M.; Möller, P. Rare-earth element systematics of the chemically precipitated component in early Precambrian iron formations and the evolution of the terrestrial atmosphere-hydrosphere-lithosphere system. *Geochim. Cosmochim. Acta.* **1993**, *57*, 2239–2249. [[CrossRef](#)]
- Bekker, A.; Planavsky, N.J.; Krapež, B.; Rasmussen, B.; Hofmann, A.; Slack, J.F.; Rouxel, O.J.; Konhauser, K.O. Iron formation: Their origins and implications for ancient seawater chemistry. In *Treatise on Geochemistry*, 2nd ed.; Mackenzie, F.T., Ed.; Elsevier: Amsterdam, The Netherlands, 2014; Volume 7, pp. 561–628.
- Czaja, A.D.; Van Kranendonk, M.J.; Beard, B.L.; Johnson, C.M. A multistage origin for Neoproterozoic layered hematite-magnetite iron formation from the Weld Range, Yilgarn Craton, Western Australia. *Chem. Geol.* **2018**, *488*, 125–137. [[CrossRef](#)]
- Robbins, L.J.; Funk, S.P.; Flynn, S.L.; Warchola, T.J.; Li, Z.; Lalonde, S.V.; Rostron, B.J.; Smith, A.J.; Beukes, N.J.; de Kock, M.O.; et al. Hydrogeological constraints on the formation of Palaeoproterozoic banded iron formations. *Nat. Geosci.* **2019**, *12*, 558–563. [[CrossRef](#)]
- Tong, X.X.; Wang, C.L.; Peng, Z.D.; Nan, J.B.; Huang, H.; Zhang, L.C. Primary mineral information and depositional models of relevant mineral facies of the early Precambrian BIF—A preliminary review. *Adv. Earth Sci.* **2018**, *33*, 152–165, (In Chinese with English abs.).
- Wang, C.L.; Konhauser, K.O.; Zhang, L.C. Depositional environment of the Paleoproterozoic Yuanjiacun Banded Iron Formation in Shanxi Province, China. *Econ. Geol.* **2015**, *110*, 1515–1539. [[CrossRef](#)]
- Berner, R.A. Authigenic mineral formation resulting from organic matter decomposition in modern sediments. *Fortschritte Mineral.* **1981**, *59*, 117–135.
- Mozley, P.S. Relation between depositional environment and the elemental composition of early diagenetic siderite. *Geology* **1989**, *17*, 704–706. [[CrossRef](#)]
- Romanek, C.S.; Jiménez-López, C.; Navarro, A.R.; Sánchez-Román, M.; Sahai, N.; Coleman, M. Inorganic synthesis of Fe–Ca–Mg carbonates at low temperature. *Geochim. Cosmochim. Acta* **2009**, *73*, 5361–5376. [[CrossRef](#)]
- Ohmoto, H.; Watanabe, Y.; Kumazawa, K. Evidence from massive siderite beds for a CO₂-rich atmosphere before ~1.8 billion years ago. *Nature* **2004**, *429*, 395–399. [[CrossRef](#)] [[PubMed](#)]
- Tice, M.M.; Lowe, D.R. Photosynthetic microbial mats in the 3416-Myr-old ocean. *Nature* **2004**, *431*, 549–552. [[CrossRef](#)] [[PubMed](#)]

15. Beukes, N.J.; Gutzmer, J. Origin and paleoenvironmental significance of major iron formations at the Archean-Paleoproterozoic boundary. *Rev. Econ. Geol.* **2008**, *15*, 5–47.
16. Heimann, A.; Johnson, C.M.; Beard, B.L.; Valley, J.W.; Roden, E.E.; Spicuzza, M.J.; Beukes, N.J. Fe, C, and O isotope compositions of banded iron formation carbonates demonstrate a major role for dissimilatory iron reduction in ~2.5 Ga marine environments. *Earth Planet. Sci. Lett.* **2010**, *294*, 8–18. [[CrossRef](#)]
17. Posth, N.R.; Köhler, I.; Swanner, E.D.; Schröder, C.; Wellmann, E.; Binder, B.; Konhauser, K.O.; Neumann, U.; Berthold, C.; Nowak, M.; et al. Simulating Precambrian banded iron formation diagenesis. *Chem. Geol.* **2013**, *362*, 66–73. [[CrossRef](#)]
18. Rasmussen, B.; Meier, D.B.; Krapez, B.; Muhling, J.R. Iron silicate microgranules as precursor sediments to 2.5-billion-year-old banded iron formations. *Geology* **2013**, *41*, 435–438. [[CrossRef](#)]
19. Halama, M.; Swanner, E.D.; Konhauser, K.O.; Kappler, A. Evaluation of siderite and magnetite formation in BIFs by pressure–temperature experiments of Fe(III) minerals and microbial biomass. *Earth Planet. Sci. Lett.* **2016**, *450*, 243–253. [[CrossRef](#)]
20. Klein, C.; Beukes, N.J. Geochemistry and sedimentology of a facies transition from limestone to iron-formation deposition in the Early Proterozoic Transvaal Supergroup, South Africa. *Econ. Geol.* **1989**, *84*, 1733–1774. [[CrossRef](#)]
21. Kaufman, A.J.; Hayes, J.M.; Klein, C. Primary and diagenetic controls of isotopic compositions of iron-formation carbonates. *Geochim. Cosmochim. Acta* **1990**, *54*, 3461–3473. [[CrossRef](#)]
22. Pecoits, E.; Gingras, M.K.; Barley, M.E.; Kappler, A.; Posth, N.R.; Konhauser, K.O. Petrography and geochemistry of the Dales Gorge banded iron formation: Paragenetic sequence, source and implications for paleo-ocean chemistry. *Precambrian Res.* **2009**, *172*, 163–187. [[CrossRef](#)]
23. Planavsky, N.J.; Asael, D.; Hofmann, A.; Reinhard, C.T.; Lalonde, S.V.; Knudsen, A.; Wang, X.; Ossa, F.O.; Pecoits, E.; Smith, A.J.B.; et al. Evidence for oxygenic photosynthesis half a billion years before the Great Oxidation Event. *Nat. Geosci.* **2014**, *7*, 283–286. [[CrossRef](#)]
24. Wittkop, C.; Teranes, J.; Lubenow, B.; Dean, W.E. Carbon-and oxygen-stable isotopic signatures of methanogenesis, temperature, and water column stratification in Holocene siderite varves. *Chem. Geol.* **2014**, *389*, 153–166. [[CrossRef](#)]
25. Garcia, T.I.; Gorton, M.P.; Li, H.; Wortmann, U.G.; Spooner, E.T. The geochemistry of the 2.75 Ga-old Helen Iron Formation, Wawa, Ontario—Insights into iron formation deposition from carbon isotopes and rare earth elements. *Precambrian Res.* **2016**, *275*, 357–368. [[CrossRef](#)]
26. Jiang, C.Z.; Tosca, N.J. Fe (II)-carbonate precipitation kinetics and the chemistry of anoxic ferruginous seawater. *Earth Planet. Sci. Lett.* **2019**, *506*, 231–242. [[CrossRef](#)]
27. Carrigan, W.J.; Cameron, E.M. Petrological and stable isotope studies of carbonate and sulfide minerals from the Gunflint Formation, Ontario: Evidence for the origin of early Proterozoic iron-formation. *Precambrian Res.* **1991**, *52*, 347–380. [[CrossRef](#)]
28. Konhauser, K.O.; Newman, D.K.; Kappler, A. The potential significance of microbial Fe (III)-reduction during Precambrian banded iron formations. *Geobiology* **2005**, *3*, 167–177. [[CrossRef](#)]
29. Johnson, C.M.; Beard, B.L.; Klein, C.; Beukes, N.J.; Roden, E.E. Iron isotopes constrain biologic and abiologic processes in banded iron formation genesis. *Geochim. Cosmochim. Acta* **2008**, *72*, 151–169. [[CrossRef](#)]
30. Johnson, C.M.; Ludois, J.M.; Beard, B.L.; Beukes, N.J.; Heimann, A. Iron formation carbonates: Paleooceanographic proxy or recorder of microbial diagenesis. *Geology* **2013**, *41*, 1147–1150. [[CrossRef](#)]
31. Craddock, P.R.; Dauphas, N. Iron and carbon isotope evidence for microbial iron respiration throughout the Archean. *Earth Planet. Sci. Lett.* **2011**, *303*, 121–132. [[CrossRef](#)]
32. Li, Y.L.; Konhauser, K.O.; Kappler, A.; Hao, X.L. Experimental low-grade alteration of biogenic magnetite indicates microbial involvement in generation of banded iron formations. *Earth Planet. Sci. Lett.* **2013**, *361*, 229–237. [[CrossRef](#)]
33. Li, W.; Beard, B.L.; Johnson, C.M. Biologically-recycled continental iron: A major component in banded iron formations. *Proc. Natl. Acad. Sci. USA* **2015**, *112*, 8193–8198. [[CrossRef](#)] [[PubMed](#)]
34. Halevy, I.; Alesker, M.; Schuster, E.M.; Popovitz-Biro, R.; Feldman, Y. A key role for green rust in the Precambrian oceans and the genesis of iron formations. *Nat. Geosci.* **2017**, *10*, 135–139. [[CrossRef](#)]
35. Köhler, I.; Konhauser, K.O.; Papineau, D.; Bekker, A.; Kappler, A. Biological carbon precursor to diagenetic siderite with spherical structures in iron formations. *Nat. Commun.* **2013**, *4*, 1–7. [[CrossRef](#)] [[PubMed](#)]
36. Tong, X.X.; Zhang, L.C.; Wang, C.L.; Peng, Z.D.; Nan, J.B. The characteristics of iron-bearing minerals and the depositional facies of BIF in Dagushan iron deposit, Anshan area: Indications of formation environment. *Acta Petrol. Sinica* **2018**, *34*, 1119–1138, (In Chinese with English abs.).
37. Song, B.; Nutman, A.P.; Liu, D.Y.; Wu, J.S. 3800 to 2500 Ma crustal evolution in the Anshan area of Liaoning Province, northeastern China. *Precambrian Res.* **1996**, *78*, 79–94. [[CrossRef](#)]
38. Wan, Y.S.; Dong, C.Y.; Xie, H.Q.; Wang, S.J.; Song, M.C.; Xu, Z.Y.; Wang, S.Y.; Zhou, H.Y.; Ma, M.Z.; Liu, D.Y. Formation Ages of Early Precambrian BIFs in the North China Craton: SHRIMP Zircon U-Pb Dating. *Acta Geol. Sinica* **2012**, *86*, 1447–1478, (In Chinese with English abs.).
39. Czaja, A.D.; Johnson, C.M.; Beard, B.L.; Roden, E.E.; Li, W.; Moorbath, S. Biological Fe oxidation controlled deposition of banded iron formation in the ca. 3770 Ma Isua Supracrustal Belt (West Greenland). *Earth Planet. Sci. Lett.* **2013**, *363*, 192–203. [[CrossRef](#)]
40. Wan, Y.S.; Ma, M.Z.; Dong, C.Y.; Xie, H.Q.; Xie, S.W.; Ren, P.; Liu, D.Y. Widespread late Neoproterozoic reworking of Meso- to Paleoproterozoic continental crust in the Anshan-Benxi area, North China Craton, as documented by U-Pb-Nd-Hf-O isotopes. *Am. J. Sci.* **2015**, *315*, 620–670. [[CrossRef](#)]

41. Zhu, M.T.; Dai, Y.P.; Zhang, L.C.; Wang, C.L.; Liu, L. Geochronology and geochemistry of the Nanfen iron deposit in the Anshan-Benxi area, North China Craton: Implications for ~2.55 Ga crustal growth and the genesis of high-grade iron ores. *Precambrian Res.* **2015**, *260*, 23–38. [[CrossRef](#)]
42. Wang, C.L.; Peng, Z.D.; Tong, X.X.; Huang, H.; Zheng, M.T.; Zhang, L.C.; Zhai, M.G. Late Neoproterozoic supracrustal rocks from the Anshan-Benxi terrane, North China Craton: New geodynamic implications from the geochemical record. *Am. J. Sci.* **2017**, *317*, 1095–1148. [[CrossRef](#)]
43. Tong, X.X.; Wang, C.L.; Peng, Z.D.; Huang, H.; Zhang, L.C.; Zhai, M.G. Geochemistry of meta-sedimentary rocks associated with the Neoproterozoic Dagushan BIF in the Anshan-Benxi area, North China Craton: Implications for their provenance and tectonic setting. *Precambrian Res.* **2019**, *325*, 172–191. [[CrossRef](#)]
44. Zhou, S.T. *Geology of the BIF in Anshan-Benxi Area*; Geological Publishing House: Beijing, China, 1994; pp. 1–277. (In Chinese)
45. Cui, P.L. Metallogenic Tectonic Setting, Metallogenic and Prospecting Models for Precambrian Iron-Formation in the Anshan-Benxi Area. Ph.D. Thesis, Jilin University, Jilin, China, 2014. (In Chinese).
46. Zhao, G.C.; Sun, M.; Wilde, S.A.; Li, S.Z. Late Archean to Paleoproterozoic evolution of the North China Craton: Key issues revisited. *Precambrian Res.* **2005**, *136*, 177–202. [[CrossRef](#)]
47. Zhang, L.C.; Zhai, M.G.; Wan, Y.S.; Guo, J.H.; Dai, Y.P.; Wang, C.L.; Liu, L. Study of the Precambrian BIF-iron deposits in the North China Craton: Progresses and questions. *Acta Pet. Sin.* **2012**, *28*, 3431–3445. (In Chinese with English abs.).
48. Li, L.X.; Li, H.M.; Liu, M.J.; Yang, X.Q.; Meng, J. Timing of deposition and tectonothermal events of banded iron formations in the Anshan-Benxi area, Liaoning Province, China: Evidence from SHRIMP U-Pb zircon geochronology of the wall rocks. *J. Asian Earth Sci.* **2016**, *129*, 276–293. [[CrossRef](#)]
49. Yang, X.Q. Master Dissertation In: Study on Iron Ore-forming Process of Metamorphic Terrain in Anshan-Benxi Area, Liaoning Province, China. Ph.D. Thesis, China University of Geosciences, Beijing, China, 2013. (In Chinese).
50. Wang, C.L.; Huang, H.; Tong, X.X.; Zheng, M.T.; Peng, Z.D.; Nan, J.B.; Zhang, L.C.; Zhai, M.G. Changing provenance of late Neoproterozoic metasedimentary rocks in the Anshan-Benxi area, North China Craton: Implications for the tectonic setting of the world-class Dataigou banded iron formation. *Gondwana Res.* **2016**, *40*, 107–123. [[CrossRef](#)]
51. Dai, Y.P. The Archean two-stage BIF deposition and genesis of high-grade iron ores in the Anshan-Benxi area. Ph.D. Thesis, University of Chinese Academy of Sciences, Beijing, China, 2014. (In Chinese).
52. Wu, F.Y.; Lin, J.Q.; Wilde, S.A.; Zhang, X.; Yang, J.H. Nature and significance of the Early Cretaceous giant igneous event in eastern China. *Earth Planet. Sci. Lett.* **2005**, *233*, 103–119. [[CrossRef](#)]
53. Zhu, X.K.; Li, Z.H.; Zhao, X.M.; Tang, S.H.; He, X.X.; Nick, S. Belshaw. High-precision measurements of Fe isotopes using MC-ICP-MS and Fe isotopic compositions of geological reference materials. *Acta Petrol. Mineral.* **2008**, *27*, 263–272. (In Chinese with English abs.).
54. Tang, S.H.; Zhu, X.K.; Cai, J.J.; Li, S.Z.; He, X.X.; Wang, J.H. Chromatographic separation of Cu, Fe and Zn using AG MP-1 Anion Exchange resin for isotope determination by MC-ICP-MS. *Rock Mineral Anal.* **2006**, *25*, 5–8.
55. Jacobsen, S.B.; Kaufman, A.J. The Sr, C and O isotopic evolution of Neoproterozoic seawater. *Chem. Geol.* **1999**, *161*, 37–57. [[CrossRef](#)]
56. Tong, X.X.; Wang, C.L.; Peng, Z.D.; Li, Y.H.; Hao, W.D.; Mänd, K.; Robbins, L.J.; Zhang, L.C.; Ke, Q.; Zhai, M.G.; et al. Depositional and environmental constraints on the late Neoproterozoic Dagushan deposit (Anshan-Benxi area, North China Craton): An Algoma-type banded iron formation. *Econ. Geol.* **2021**, in press.
57. Ayres, D. Genesis of iron-bearing minerals in banded iron formation mesobands in the Dales Gorge Member, Hamersley Group, Western Australia. *Econ. Geol.* **1972**, *67*, 1214–1233. [[CrossRef](#)]
58. Klein, C. Some Precambrian banded iron-formations (BIFs) from around the world: Their age, geologic setting, mineralogy, metamorphism, geochemistry, and origin. *Am. Mineral.* **2005**, *90*, 1473–1499. [[CrossRef](#)]
59. Tang, D.; Shi, X.; Jiang, G.; Wu, T.; Ma, J.; Zhou, X. Stratiform siderites from the Mesoproterozoic Xiamaling Formation in North China: Genesis and environmental implications. *Gondwana Res.* **2018**, *58*, 1–15. [[CrossRef](#)]
60. Ewers, W.; Morris, R. Studies of the Dales Gorge Member of the Brockman Iron Formation, Western Australia. *Econ. Geol.* **1981**, *76*, 1929–1953. [[CrossRef](#)]
61. Shields, G.; Veizer, J. Precambrian marine carbonate isotope database: Version 1.1. *Geochem. Geophys. Geosyst.* **2002**, *3*. [[CrossRef](#)]
62. Eglinton, B.M.; Talma, A.S.; Marais, S.; Matthews, P.E.; Dixon, J.G.P. Isotopic composition of Pongola Supergroup limestones from the Buffalo River gorge, South Africa: Constraints on their regional depositional setting. *S. Afr. J. Geol.* **2003**, *106*, 1–10. [[CrossRef](#)]
63. Beukes, N.J.; Klein, C. Geochemistry and sedimentology of a facies transition—From microbanded to granular iron-formation—In the early Proterozoic Transvaal Supergroup, South Africa. *Precambrian Res.* **1990**, *47*, 99–139. [[CrossRef](#)]
64. Beukes, N.J.; Klein, C.; Kaufman, A.J.; Hayes, J.M. Carbonate petrography, kerogen distribution, and carbon and oxygen isotope variations in an Early Proterozoic transition from limestone to iron-formation deposition: Transvaal Supergroup, South Africa. *Econ. Geol.* **1990**, *85*, 663–690. [[CrossRef](#)]
65. Kaufman, A.J. Geochemical and mineralogic effects of contact metamorphism on banded iron-formation: An example from the Transvaal Basin, South Africa. *Precambrian Res.* **1996**, *79*, 171–194. [[CrossRef](#)]
66. Sumner, D.Y. Carbonate precipitation and oxygen stratification in Late Archean seawater as deduced from facies and stratigraphy of the Gamohaam and Frisco formations, Transvaal Supergroup, South Africa. *Am. J. Sci.* **1997**, *297*, 455–487. [[CrossRef](#)]

67. Fischer, W.W.; Schröder, S.; Lacassie, J.P.; Beukes, N.J.; Goldberg, T.; Strauss, H.; Horstmann, U.E.; Schrag, D.P.; Knoll, A.H. Isotopic constraints on the Late Archean carbon cycle from the Transvaal Supergroup along the western margin of the Kaapvaal Craton, South Africa. *Precambrian Res.* **2009**, *169*, 15–27. [[CrossRef](#)]
68. Jimenez-Lopez, C.; Christopher, S.R. Precipitation kinetics and carbon isotope partitioning of inorganic siderite at 25 C and 1 atm. *Geochim. Cosmochim. Acta* **2004**, *68*, 557–571. [[CrossRef](#)]
69. Wiesli, R.A.; Beard, B.L.; Johnson, C.M. Experimental determination of Fe isotope fractionation between aqueous Fe (II), siderite and “green rust” in abiotic systems. *Chem. Geol.* **2004**, *211*, 343–362. [[CrossRef](#)]
70. Anbar, A.D.; Jarzecki, A.A.; Spiro, T.G. Theoretical investigation of iron isotope fractionation between Fe (H₂O)₆³⁺ and Fe (H₂O)₆²⁺: Implications for iron stable isotope geochemistry. *Geochim. Cosmochim. Acta* **2005**, *69*, 825–837. [[CrossRef](#)]
71. Blanchard, M.; Poitrasson, F.; Méheut, M.; Lazzeri, M.; Mauri, F.; Balan, E. Iron isotope fractionation between pyrite (FeS₂), hematite (Fe₂O₃) and siderite (FeCO₃): A first-principles density functional theory study. *Geochim. Cosmochim. Acta* **2009**, *73*, 6565–6578. [[CrossRef](#)]
72. Schauble, E.A.; Rossman, G.R.; Taylor, H.P. Theoretical estimates of equilibrium Fe isotope fractionations from vibrational spectroscopy. *Geochim. Cosmochim. Acta* **2001**, *65*, 2487–2497. [[CrossRef](#)]
73. Mortimer, R.J.; Coleman, M.L. Microbial influence on the oxygen isotopic composition of diagenetic siderite. *Geochim. Cosmochim. Acta* **1997**, *61*, 1705–1711. [[CrossRef](#)]
74. Konhauser, K.O. Diversity of bacterial iron mineralization. *Earth Sci. Rev.* **1998**, *43*, 91–121. [[CrossRef](#)]
75. Gäb, F.; Ballhaus, C.; Siemens, J.; Heuser, A.; Lissner, M.; Geisler, T.; Garbe-Schönberg, D. Siderite cannot be used as CO₂ sensor for Archean atmospheres. *Geochim. Cosmochim. Acta* **2017**, *214*, 209–225. [[CrossRef](#)]
76. Teixeira, N.L.; Caxito, F.A.; Rosière, C.A.; Pecoits, E.; Vieira, L.; Frei, R.; Sial, A.N.; Poitrasson, F. Trace elements and isotope geochemistry (C, O, Fe, Cr) of the Cauê iron formation, Quadrilátero Ferrífero, Brazil: Evidence for widespread microbial dissimilatory iron reduction at the Archean/Paleoproterozoic transition. *Precambrian Res.* **2017**, *298*, 39–55. [[CrossRef](#)]
77. Beard, B.L.; Handler, R.M.; Scherer, M.M.; Wu, L.; Czaja, A.D.; Heimann, A.; Johnson, C.M. Iron isotope fractionation between aqueous ferrous iron and goethite. *Earth Planet. Sci. Lett.* **2010**, *295*, 241–250. [[CrossRef](#)]
78. Johnson, C.M.; Roden, E.E.; Welch, S.A.; Beard, B.L. Experimental constraints on Fe isotope fractionation during magnetite and Fe carbonate formation coupled to dissimilatory hydrous ferric oxide reduction. *Geochim. Cosmochim. Acta* **2005**, *69*, 963–993. [[CrossRef](#)]
79. Crosby, H.A.; Johnson, C.M.; Roden, E.E.; Beard, B.L. Coupled Fe(II)-Fe(III) electron and atom exchange as a mechanism for Fe isotope fractionation during dissimilatory iron oxide reduction. *Environ. Sci. Technol.* **2005**, *39*, 6698–6704. [[CrossRef](#)] [[PubMed](#)]
80. Crosby, H.A.; Roden, E.E.; Johnson, C.M.; Beard, B.L. The mechanisms of iron isotope fractionation produced during dissimilatory Fe(III) reduction by *Shewanella putrefaciens* and *Geobacter sulfurreducens*. *Geobiology* **2007**, *5*, 169–189. [[CrossRef](#)]
81. Rouxel, O.J.; Bekker, A.; Edwards, K.J. Iron Isotope Constraints on the Archean and Paleoproterozoic Ocean Redox State. *Science* **2005**, *307*, 1088–1091. [[CrossRef](#)] [[PubMed](#)]
82. Heard, A.W.; Dauphas, N. Constraints on the coevolution of oxic and sulfidic ocean iron sinks from Archean–Paleoproterozoic iron isotope records. *Geology* **2020**, *48*, 358–362. [[CrossRef](#)]
83. Ossa, F.O.; Hofmann, A.; Wille, M.; Spangenberg, J.E.; Schoenberg, R. Aerobic iron and manganese cycling in a redox-stratified mesoarchean epicontinental sea. *Earth Planet. Sci. Lett.* **2018**, *500*, 28–40. [[CrossRef](#)]
84. Konhauser, K.O.; Amskold, L.; Lalonde, S.V.; Posth, N.R.; Kappler, A.; Anbar, A. Decoupling photochemical Fe(II) oxidation from shallow-water BIF deposition. *Earth Planet. Sci. Lett.* **2007**, *258*, 87–100. [[CrossRef](#)]
85. Chester, R. *Marine Geochemistry*, 2nd ed.; Blackwell Publishing: Oxford, UK, 2003.
86. Dauphas, N.; van Zuilen, M.; Busigny, V.; Lepland, A.; Wadhwa, M.; Janney, P.E. Iron isotope, major and trace element characterization of early Archean supracrustal rocks from SW Greenland: Protolith identification and metamorphic overprint. *Geochim. Cosmochim. Acta* **2007**, *71*, 4745–4770. [[CrossRef](#)]
87. Becker, R.H.; Clayton, R.N. Carbon isotopic evidence for the origin of a banded iron-formation in Western Australia. *Geochim. Cosmochim. Acta* **1972**, *36*, 577–595. [[CrossRef](#)]
88. Yang, X.; Zhang, Z.; Santosh, M.; Duan, S.; Liang, T. Anoxic to suboxic Mesoproterozoic ocean: Evidence from iron isotope and geochemistry of siderite in the Banded Iron Formations from North Qilian, NW China. *Precambrian Res.* **2018**, *307*, 115–124. [[CrossRef](#)]